Origin of compression-induced failure in brittle solids under shock loading

J. Y. Huang, Y. Li, Q. C. Liu, X. M. Zhou, L. W. Liu, C. L. Liu, M. H. Zhu, and S. N. Luo

Origin of compression-induced failure in brittle solids under shock loading

J. Y. Huang,[1,2] Y. Li,[2] Q. C. Liu,[2] X. M. Zhou,[2] L. W. Liu,[3] C. Liu,[3] M. H. Zhu,[4,*] and S. N. Luo[2,†]

[1]*CAS Key Laboratory of Materials Behavior and Design, Department of Modern Mechanics, University of Science and Technology of China, Hefei, Anhui 230027, P. R. China*

[2]*The Peac Institute of Multiscale Sciences, Chengdu, Sichuan 610031, P. R. China*

[3]*Institute of Fluid Physics, Mianyang, Sichuan 621900, P. R. China*

[4]*Key Laboratory of Advanced Technologies of Materials, Ministry of Education, Southwest Jiaotong University, Chengdu, Sichuan 610031, P. R. China*

(Dated: September 14, 2015)

Abstract

The origin of compression-induced failure in brittle solids has been a subject of debate. Using *in situ*, high-speed, strain field mapping of a representative material, polymethylmethacrylate, we reveal that shock loading leads to heterogeneity in compressive strain field, which in turn gives rise to localized lateral tension and shear through Poisson's effects, and subsequently, localized microdamage. A failure wave nucleates from the impact surface and its propagation into the microdamage zone is self-sustained, and triggers interior failure. Its velocity increases with increasing shock strength and eventually approaches the shock velocity. The seemingly puzzling phenomena observed in previous experiments, including incubation time, failure wave velocity variations, and surface roughness effects, can all be explained consistently with nucleation and growth of microdamage, and the effects of loading strength and preexisitng defects.

PACS numbers: 62.20.M-, 81.05.Lg, 42.15.Dp

I. INTRODUCTION

Compression failure of brittle solids, including glasses, polymers, ceramics and rocks, under impulsive loading is of broad interest to materials science, shock physics, and impact and earthquake engineering[1–4]. A self-propagating fracture front in brittle solids has long been observed during high-speed impact[5], and was first termed as "failure wave" by Rasorenov et al.[6] based on free surface velocity measurements on glasses. Subsequently, Bourne et al.[3] provided visual evidence for failure waves in a glass under shock compression with high-speed photography.

Several mechanisms have been proposed to explain failure wave nucleation and propagation in brittle solids during compression, including the advancement of surface cracks[6,7], shear-induced cracking[8], and phase transition[9]. However, those mechanisms are inconclusive in the absence of direct experimental verification. The phase-transition mechanism is disputed since no phase transition occurs in glasses below the Hugoniot elastic limit[10,11]. Bourne et al.[7] and Raiser et al.[12] examined the effects of surface roughness on the nucleation of failure waves but drew contradictory conclusions. In addition, the crack advancement mechanism cannot predict a failure wave velocity approaching that of a shock wave[3,13], since the maximum crack velocity is limited by the Rayleigh wave speed[14,15]. Shear-induced cracking provides a general micromechanical picture for failure waves[3], but remains to be confirmed experimentally, and it cannot explain why failure waves generally initiate at the impact surface. Direct measurements on the stress/strain fields behind the shock front are still challenging. For instance, the widely used stress gauges[7] provide only an integrated response over the gauge area, typically on the order of 1 mm^2 .

Previously, the failure wave velocity (U_{f}) was deduced from free-surface particle velocity profiles, assuming immediate activation of failure by a shock[16]. However, the validity of this assumption is still under debate[17], since incubation time for failure nucleation needs to be considered for calculating U_{f}. Steady failure wave propagation was observed at a given stress level[3,18], whereas decelerating failure waves were also reported[19]. Another dispute is the dependence of U_{f} on loading stress, which is either negligible[18] or considerable[3].

High-speed photography is useful for imaging damage[20,21], since the transparency behind a failure front decreases due to light scattering incurred by small-scale fracture and fragmentation. The micro- or mesoscale stress and strain distributions behind a shock front
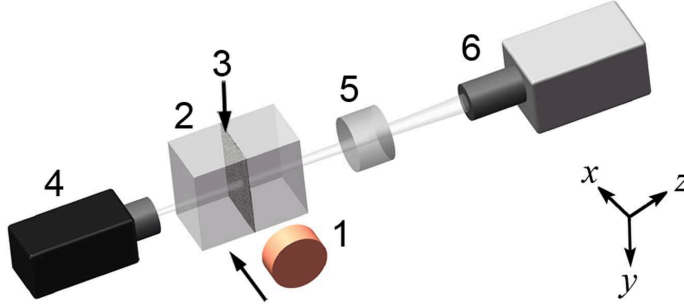
FIG. 1. Schematic setup for impact loading and high-speed photography. 1: flyer plate; 2: PMMA sample; 3: a thin layer of C particles; 4: light source; 5: lens; 6: high-speed ICCD camera. The x- and z-axes are along the impact and viewing directions, respectively.

are important for revealing the physical origin of failure waves, but *in situ*, real-time, such measurements under shock loading are extremely rare. High-speed digital image correlation (DIC) has become an established technique for full-field strain measurements in a wide variety of applications[22,23]. Here, we utilize high-speed DIC to dynamically map the strain fields at fine scales in a model material, polymethylmethacrylate or PMMA, during shock loading. We reveal that shock compression induces heterogeneity in compressive deformation, which consequently leads to localized tension and shear behind the shock front, and compression-induced failure in brittle solids. In fact, extensive studies have been devoted to propagation of a single crack, such as crack velocity and fracture energy, in PMMA with notched samples[15,24–27]. Comparison and discussions with those insightful results are also presented.

II. METHODOLOGY

A schematic diagram of the experimental setup, including impact loading and high-speed photography systems, is presented in Fig. 1. The impact velocity is measured within 1% by an optical beam blocking system. A six-frame ICCD camera is used for high-speed photography, with a xenon lamp as illumination. A coaxial shorting pin is attached to the sample to supply a trigger signal for synchronizing the impact and the camera. Proper delays to the camera trigger are implemented with a digital delay/pulse generator.

The flyer plates are made of oxygen-free high purity Cu, and the samples, optical-quality

PMMA. The impact surfaces of the flyer plates and PMMA samples are mirror-finished, and their roughnesses, evaluated by the root mean square (RMS), are 18.2±5.3 nm and 21.4±5.8 nm, respectively, measured with the atomic force microscopy. The diameter and thickness of the flyer plates are 14 mm and 4 mm, respectively. The sample thickness is 10 mm, and the dimensions of the impact surface are 15 mm×15 mm. The samples are fabricated from the same batch of PMMA, and divided into two groups: non-DIC and DIC samples. A non-DIC sample is a whole piece of PMMA. Each DIC sample consists of two identical, mirror-finished, pieces (7.5 mm×15 mm×10 mm). A small amount of C particles (∼8 μm in diameter) are mixed with an adhesive (the optimum mass ratio is about 1:2) . The two pieces are then bonded with the adhesive, forming a 15 mm×15 mm×10 mm sample with a thin layer of C particles (38±18 μm thick) sandwiched between. The adhesive layer has negligible effect as demonstrated by previous experiments using embedded stress gauges[7,16]. We also perform validation shots with the adhesive layer parallel to the loading direction, and observe that deformation of the particle layer is indistinguishable from that of its surroundings and has little influence on the propagation of the shock and failure waves. The light transmitted through the sample along the z-axis is relayed through a magnifying lens into the camera recording image sequences. The spatial resolution is approximately 14 μm. The C particles produce speckles under xenon lamp illumination required for DIC analysis.

Impact experiments are conducted on non-DIC and DIC samples. The non-DIC shots are intended to measure simultaneously shock wave and failure wave velocities, while the DIC shots, also for strain field mapping. The Green-Lagrangian strain tensor is calculated from the displacement (u) gradients as

$$E_{ij} = \frac{1}{2}\left(u_{i,j} + u_{j,i} + u_{k,i}u_{k,j}\right), \tag{1}$$

where i, $j = x$, y. Correlation is done between a dynamic image (after loading) and its static counterpart (before loading).

III.   RESULTS AND DISCUSSIONS

Plate impact experiments are conducted on a single-stage gas gun at impact velocities of 0.11–0.56 km s^{-1}. The tilt angle measured using multiple DPS (Doppler pin system) probes
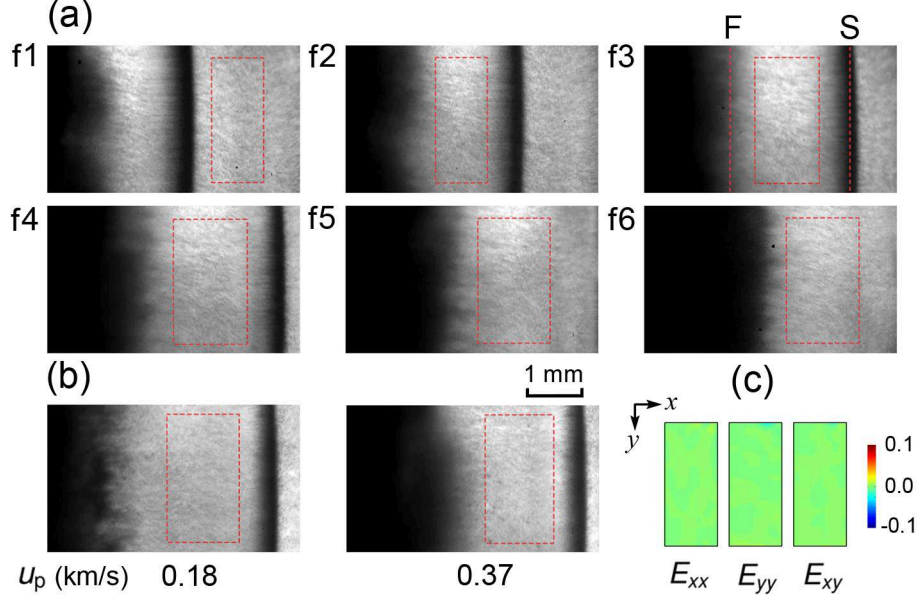
FIG. 2. (a) High-speed photographs of PMMA for particle velocity $u_p = 0.28$ km s^{-1}. The exposure time is 20 ns, and the intervals between neighboring frames (f1–f6) are 200 ns. The dashed rectangles denote the regions of interest (ROI) for DIC. F and S refer to the failure and shock wave fronts, respectively. (b) Snapshots for $u_p = 0.18$ and 0.37 km s^{-1} at 1.5 μs after the impact [corresponding to frame f4 in (a)]. (c) Strain fields before the shock front, corresponding to ROI in frame f1 in (a). No significant strains exist prior to the shock front as expected which verifies the DIC analysis.

is about 6 mrad. Some representative snapshots are shown in Figs. 2(a) and 2(b). The field of view and regions of interest (ROI) for DIC (dashed rectangles) are selected to avoid edge effects. The wave propagation for an impact velocity of 0.31 km s^{-1} ($u_p = 0.28$ km s^{-1}) is shown in the high-speed photographs [Fig. 2(a)]. The shock front (dark stripe) propagates across the sample along the impact direction. Darkening of the shock front is caused by the index of refraction gradient, which is in turn due to the density gradient on shock rise[3]; transparency recovers behind the shock front when a steady Hugoniot state is achieved with vanishing gradients in index of refraction. Deformation in the glue layer cannot account for such darkening due to its small thickness (38 μm).

A failure wave nucleates from the impact surface and then propagates into the interior, lagging behind the shock front. As time evolves, the failure wave front becomes rough; discrete damage sites can be seen behind the failure wave front, where heterogeneous fracture
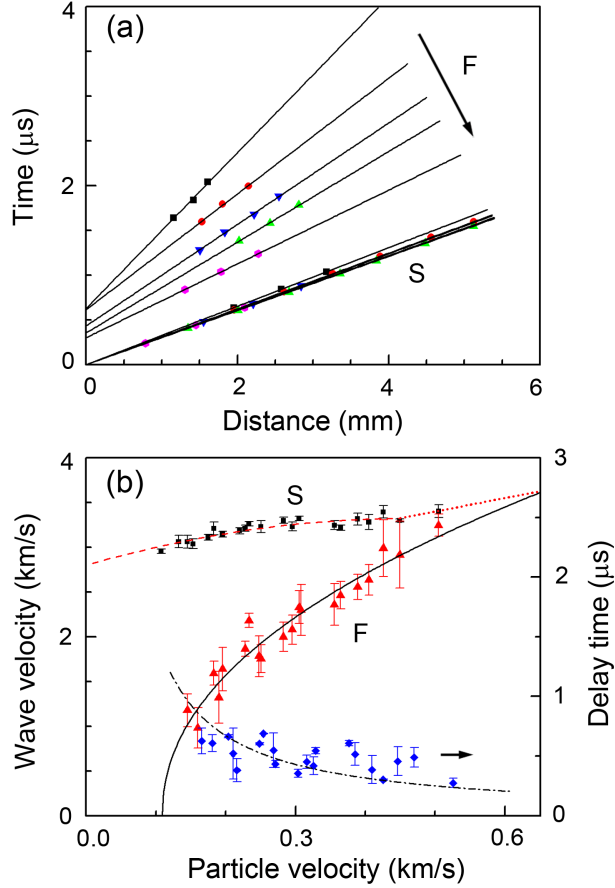
FIG. 3. (a) The position–time (x–t) diagram of the shock (S) and failure (F) wave fronts at representative shock strengths. The arrow denotes increasing particle velocity. (b) Shock and failure wave velocities, and delay time τ_d versus particle velocity in PMMA. The dashed[28] and dotted[29] curves denote independent measurements. The solid curve and dash-dot curve are the fitting to failure wave velocity and delay time, respectively.

occurs. For PMMA, there is no well defined elastic-plastic transition[28]; the failure waves observed in our experiments, lagging behind the shock wave by 300–700 ns (see below), should not be interpreted as a plastic wave. However, the failure wave causes obvious change in the optical property of PMMA (darkening), but may not cause appreciable particle velocity variations in materials[28]. Our particle velocity history measurements (at both the impact surface, and the sample/window interface) are similar to those of Barker and Hollenbach[28], but do not exhibit distinct features for failure waves. To validate the DIC analysis, we examine the ROI of frame 1 in Fig. 2(a), a region before the shock front. The normal strain (E_{xx}, E_{yy}), and shear strain (E_{xy}) fields all show strain values around zero as expected [Fig. 2(c)],

with some negligible noise (0.005) intrinsic to this method.

At a given instant (t), the positions (x) of the shock and failure wave fronts are obtained from averaging the respective leading edges; the trajectories for representative shots (21 shots in total) are presented in the x–t diagram [Fig. 3(a)], from which the shock (U_s) and failure (U_f) wave velocities are deduced [see Fig. 3(b)]. The particle velocity u_p and shock pressure in PMMA can be calculated via impedance match, given U_s in the target, the impact velocity, and the U_s–u_p relation for the impactor[29], $U_s = 3.94 + 1.49u_p$ in km s^{-1}. Since the impedance of Cu is much higher than that of PMMA, the particle velocity is actually close to the impact velocity in our experiments. Our U_s–u_p data for PMMA shown in Fig. 3(b) are in excellent agreement with independent measurements from Barker and Hollenbach[28] (dashed line), and Marsh[29] (dotted line) in the pressure range explored.

The failure waves are not generated simultaneously with the shock upon impact, but with a delay, τ_d, of 300–700 ns for various impact velocities (Fig. 3). Therefore, a finite incubation time is necessary to initiate dynamic fracture, and subsequently, a propagating failure wave. τ_d decreases slightly when impact velocity increases [Fig. 3(b)], but with large fluctuations due to measurement errors. A power law is used to fit the decreasing trend of delay time with particle velocity : $\tau_d = \tau_d^0 \left(u_p/u_p^0\right)^\beta$, where $\tau_d^0 = 449$ ns, $u_p^0 = 0.35$ km s^{-1}, and $\beta = -0.38$. Similar phenomena were observed in soda lime glass[17] and rocks[13].

Consistent with previous experiments[16], U_f increases with increasing u_p [Fig. 3(b)], and can be described with

$$U_f = U_f^0 \left(\frac{u_p}{u_p^0} - 1\right)^\alpha. \tag{2}$$

Here the fitting parameters $U_f^0 = 1.71 \pm 0.05$ km s^{-1}, $u_p^0 = 0.11 \pm 0.01$ km s^{-1}, and $\alpha = 0.47 \pm 0.03$. u_p^0 is the minimum or threshold particle velocity beyond which a failure wave can initiate (corresponding to a shock pressure of 0.32 GPa). We have explored low impact velocities, e.g. 0.118 km s^{-1} (corresponding u_p=0.10 km/s), where the evolution of a failure wave is not recognizable and only shock wave propagation is observed. U_f increases faster with increasing shock strength than U_s so that the failure wave catches up with the shock wave at $u_p \sim 0.65$ km s^{-1}. The failure wave velocity exceeds the maximum crack velocity generally observed in PMMA, typically 0.6 times the Rayleigh wave speed[15], because considering that the failure wave is not propagation of a single crack but a failure front (likely crack networks[8]), to which the elastic fracture mechanics theory is inapplicable[24]. In
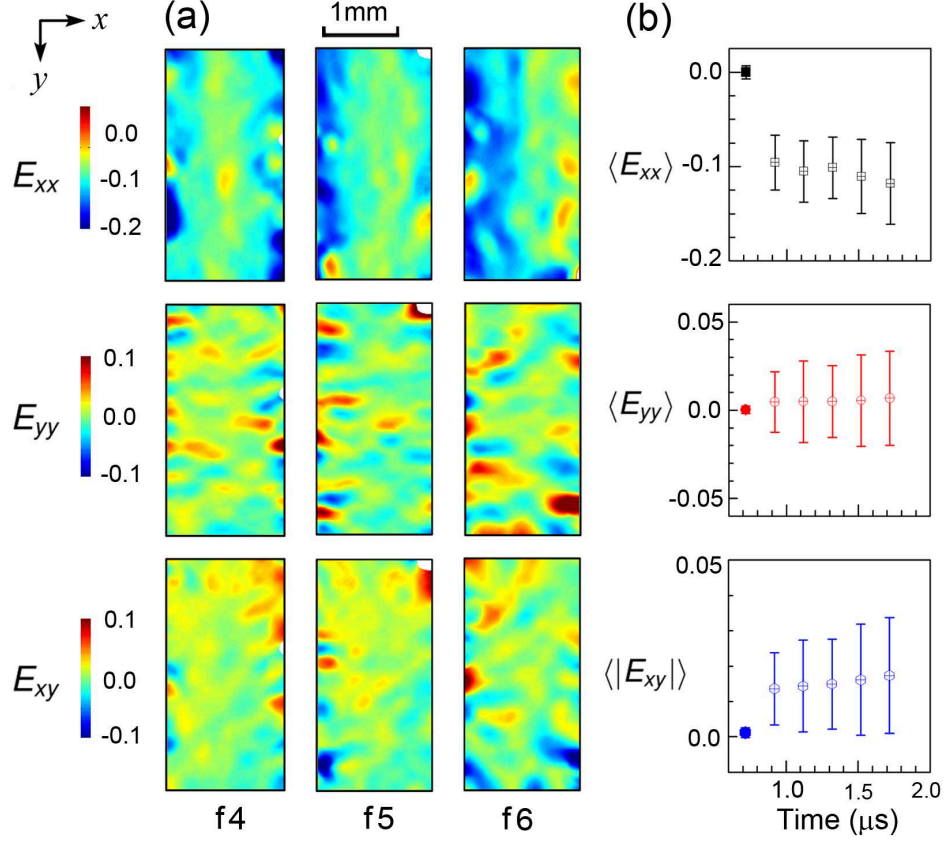
7

FIG. 4. Strain evolutions for $u_{\mathrm{p}} = 0.28 \ \mathrm{km \, s^{-1}}$, corresponding to frames f1–f6 in Fig. 2(a). (a) Normal (E_{xx}, E_{yy}) and shear (E_{xy}) strain fields in the intermediate region between the shock and failure wave fronts at f4–f6. (b) Area-averaged strain: $\langle E_{xx} \rangle$, $\langle E_{yy} \rangle$, and $\langle |E_{xy}| \rangle$. The filled symbols denote preshock values [ROI in frame f1, Fig. 2(a)].

addition, the material before the failure front is predamaged by shock compression (Figs. 4 and 5) which reduces the energy barrier to failure and promotes the failure wave velocity. Actually, super-shear rupture has also been observed in frictionally held interfaces and faults[1,30].

The failure wave front is generally rough (as opposed to the clean shock front), and propagates approximately at a constant velocity; the region behind it also displays various heterogeneities. However, the region between the shock and failure wave fronts, or simply the intermediate region, seems to be "intact" but may play a role in damage and failure wave propagation. We thus resort to DIC analysis to reveal possible, visually undetectable, microdamage, which reduces the energy barrier to visually observable fracture triggered by the arrival of a failure wave. We obtain 2D strain fields within the intermediate region for

different $u_{\rm p}$ (Figs. 4 and 5). The strain field maps of E_{xx}, E_{yy}, and E_{xy} for $u_{\rm p} = 0.28~{\rm km\,s}^{-1}$ at different time are shown in Fig. 4(a), and the area-averaged strain values, $\langle E_{xx} \rangle$, $\langle E_{yy} \rangle$, and $\langle |E_{xy}| \rangle$, in Fig. 4(b).

A key feature of the strain field maps is the pronounced mesoscale heterogeneities, i.e., strain localizations in the intermediate regions under bulk 1D-strain loading. $E_{xx}(x,y)$ shows mainly negative values and thus compression, consistent with the bulk loading condition. The heterogeneity in compression deformation, indicated by the large variances in $\langle E_{xx} \rangle$ [error bars in Fig. 4(b)], could be attributed to the inherent micro structures of PMMA, including tangled and crosslinked molecular chains and clusters[31] or microdefects, although the exact nature of structural heterogeneity remains to be investigated. Such structural heterogeneities are more marked in heterogeneous materials including rocks[13], composites[32], and multiphase alloys[23]. Similarly, crazing observed in brittle polymers at highly stressed regions has been associated with molecular inhomogeneities[33,34]. Lawn[35] introduced a concept of "energy sinks" (e.g. second-phase particles) to explain formation of micro cracks before the crack tip when the crack velocity exceeds certain critical value. Each "energy sink" grows into a micro crack when it is properly located and the local stress exceeds some yield stress[26], consistent with our explanation. Moreover, micro cracking or damage also augments the heterogeneity in strain fields.

In $E_{yy}(x,y)$ and $E_{xy}(x,y)$, we observe random-shaped, alternating, positive and negative, zones. A finite E_{yy} value is mainly resulted from Poisson's effect (Poisson's ratio of PMMA is 0.42[36]). The area-averaged $\langle E_{yy} \rangle$ is much smaller ($\sim 0.5\%$) than $\langle E_{xx} \rangle$ due to transient lateral confinement. However, pronounced localization in tension is induced in the lateral direction, in response to strain heterogeneity in compression along the loading direction. The heterogeneities in $E_{xx}(x,y)$ and $E_{yy}(x,y)$ then give rise to that in $E_{xy}(x,y)$. $\langle E_{xx} \rangle$, $\langle E_{yy} \rangle$, and $\langle |E_{xy}| \rangle$ and their variances increase slightly with time [Fig. 4(b)], because of stress relaxations[8]. Since a certain amount of tensile and shear strain energy is stored in the material through corresponding strain localization, the microdamage behind the shock front reduces significantly the energy barrier to failure[37], thus supporting a stable propagation of failure waves.

The von Mises equivalent strain[38] can be calculated from the strain components as

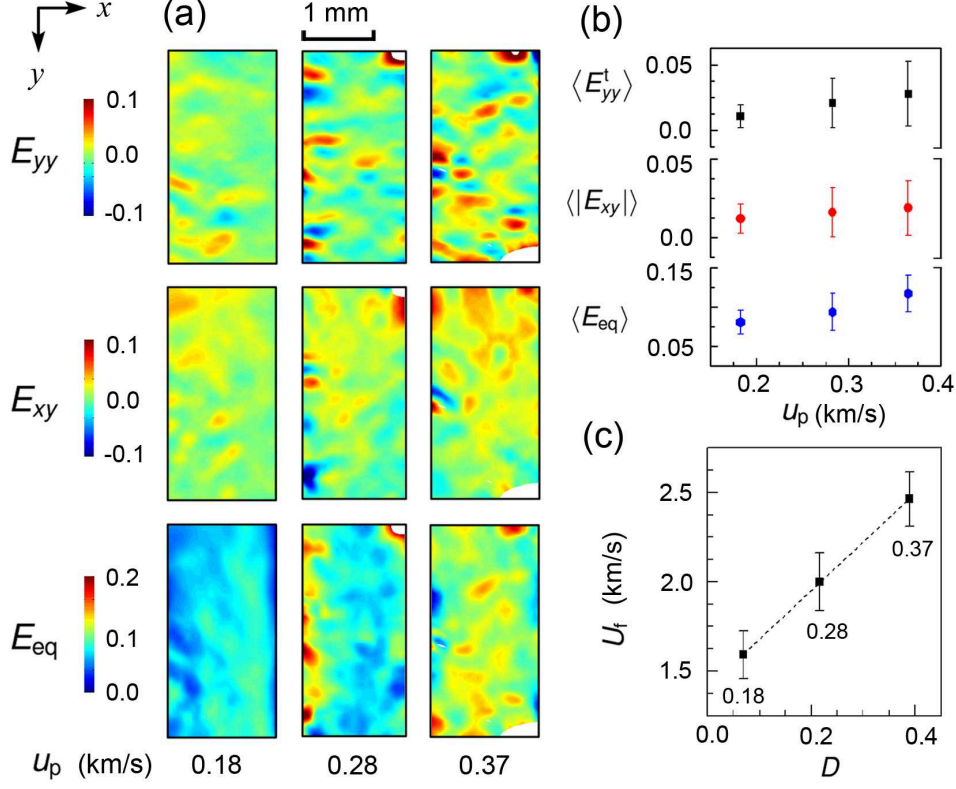$$E_{\rm eq} = \frac{\sqrt{2}}{3} \left[E_{xx}^2 + E_{yy}^2 + (E_{xx} - E_{yy})^2 + 6E_{xy}^2 \right]^{\frac{1}{2}}.\tag{3}$$

FIG. 5. Compression-induced microdamage via lateral tension and shear at different u_{p}. (a) $E_{yy}(x,y)$, $E_{xy}(x,y)$, and $E_{\mathrm{eq}}(x,y)$ for ROIs in f4, Fig. 2(a) and in Fig. 2(b). (b) Corresponding area-averaged strain, $\langle E_{yy}^{\mathrm{t}} \rangle$, $|\langle E_{xy} \rangle|$, and $\langle E_{\mathrm{eq}} \rangle$, at different u_{p}. Superscript t in $\langle E_{yy}^{\mathrm{t}} \rangle$ indicates that only tension (positive E_{yy}) is considered. (c) U_{f} versus damage (D). Numbers denote u_{p} in km s^{-1}.

The strain field maps, $E_{xx}(x,y)$, $E_{yy}(x,y)$, $E_{xy}(x,y)$ and $E_{\mathrm{eq}}(x,y)$, at different u_{p} are obtained [Fig. 5(a)]. E_{xx} is not presented since it is not directly related to damage as opposed to tension and shear[8,39]. Correlation is poor in the white patches. The corresponding area-averaged values, $\langle E_{yy}^{\mathrm{t}} \rangle$, $|\langle E_{xy} \rangle|$, and $\langle E_{\mathrm{eq}} \rangle$, are shown in Fig. 5(b) for three representative shock strengths. Superscript t in $\langle E_{yy}^{\mathrm{t}} \rangle$ indicates that only tension (positive E_{yy}) is considered. The maximum and mean values of tensile, shear and equivalent strain, as well as their spatial variations as indicated by the variances, increase considerably with increasing u_{p}. Moreover, strain localization increases in both locality and amplitude. Such tension and shear localizations turn into discrete microdamage nucleation sites (nuclei), growing into the damage zones behind the failure wave front [Fig. 2(a)]. The shear strain fields also show multiple intersecting bands, confirming that shear cracking plays an important role in the

10

nucleation of compression-induced failure in brittle solids[40,41].

The maximum tensile and shear strain sustained in PMMA under dynamic tensile and shear loading are about 0.025 and 0.035, respectively[42,43]. Above these threshold values, micro tensile or shear cracks (microdamage) appear. We then define the damage parameter (D) in an ROI as the area fraction of the pixels with a strain value above either the tensile or shear strain threshold value, i.e., microdamage is quantified in terms of compression-induced, tension or shear concentrations. Figure 5(c) reveals an increase of D with increasing u_{p}, and with increasing U_{f}. Therefore, the appreciable increase in failure wave velocity with increasing shock strength [Fig. 3(b)] is attributed to increasing microdamage behind the shock front. Similarly, micro cracks before the crack tip[26,27] are very likely activated through localized deformation induced by local stress concentrations, physically consistent with micro damage in our work. However, micro crack branching[24] introduces new dissipation mechanisms and sets limit to the propagation speed of single cracks[26]. On the other hand, micro damage proposed here is induced by heterogeneous shock compression and can thus facilitate failure wave propagation. In addition, coalescence of micro cracks (before the crack tip) leaves conic marks in the postmortem fracture surfaces[26,27] while samples under planar impact loading fracture into pieces behind the failure wave.

Failure usually initiates from the impact surface driven by compression-induced, localized, tension and shear, since there are inevitably more defects on the surface than in the interior, and the impact surface is shock-compressed before the interior. At low shock strengths above u_{p}^{0}, the nucleation rate and amplitude of microdamage are low, and it takes finite time, or an incubation period (τ_{d}), for the microcracks to grow and coalesce into failure. Thus, a delay time τ_{d} of 300–700 ns is observed for various u_{p} [Fig. 3(b)]. Once initiated, the failure wave can propagate steadily forward into the "predamaged" intermediate region with slowly growing nuclei produced by shock compression, leaving failure behind. This provides a reasonable micro mechanism for the so-called self-sustained failure propagation model[44]. With increasing shock strength, the incubation time decreases and the failure wave velocity increases, since more nucleation sites and more damage are produced by shock compression, and the growth dynamics is accelerated under enhanced driving force (Fig. 4). The propagation of surface cracks itself cannot lead to U_{f} approaching the shock velocity[13], and the predamage induced by shock compression facilitates failure upon the arrival of the failure wave[45].

At high shock strengths (e.g., $u_p = 0.65$ km s^{-1}), the failure wave catches up with the shock wave [Fig. 3(b)]. Inferred from Fig. 5(c), the nucleation rate of microdamage induced by local tension and shear behind the shock front becomes sufficiently large, and their growth dynamics becomes sufficiently fast, so failure is incurred via catastrophic self-growth. The trigger role of a propagating failure wave initiated from the impact surface is of less importance in such cases because the growth of nuclei is spontaneous, and they connect to form a failure zone without resorting to the boost of a failure wave. The failure wave is no longer a propagating wave, and the apparent failure wave velocity approaches the shock wave velocity in this extreme case, consistent with previous observations on rocks[13]. With increasing shock strength, the failure wave front trajectory becomes parallel to the shock front trajectory, but shifts upward in the $x-t$ diagram since a finite incubation time is still required (Fig. 3). A rough surface with a large number of microcracks may reduce the incubation time to essentially zero. As a result, incubation time is observed in some experiments[13,17] including this work, but not in some other cases[3,10]. However, for stronger brittle materials such as fused quartz[19], shock compression may not induce sufficient tension and shear localization or microdamage behind the shock front, so the increase in U_f is negligible in the shock strength range explored[18]. This explains the contradictory observations on failure wave velocities (see Introduction). For heterogenous materials such as rocks, the preexisting defects and interfaces reduce the energy barrier and facilitate the failure dynamics, reducing the incubation time and increasing the failure wave velocity, which also approaches the shock wave velocity[13].

IV. CONCLUSION

In summary, the origin of compression-induced failure in brittle solids under shock compression is revealed as compression-induced localization of lateral tension and shear. Shock compression yields heterogeneous compression strain fields owing to intrinsic structural heterogeneity at micro- or mesoscales, and localized tension follows in the lateral direction due to Poisson's effect, although the bulk lateral strain remains around zero given transient lateral confinement. Lateral tension is accompanied by shear. A failure wave is initiated from the impact surface, and triggers the failure of the predamaged zone, and its propagation is self-sustained. Compression-induced predamage and failure wave velocity increase as

12

shock strength increases, and failure wave-triggered failure transits to catastrophic growth in the extreme case where the failure wave catches up with the shock wave. The preexisting defects simply reduce the threshold impact velocity, facilitate damage dynamics and increase failure wave velocity. The seemingly conflicting phenomena observed in previous experiments, including incubation time[17], failure wave velocity variations[18,46], and surface roughness effects[7,12], can all be explained consistently with nucleation and growth of microdamage, and the effects of loading strength and preexisitng defects.

---

* zhuminghao@swjtu.cn

† sluo@pims.ac.cn

1 K. Xia, A. J. Rosakis, and H. Kanamori, Science **303**, 1859 (2004).

2 F. Kun, I. Varga, S. Lennartz-Sassinek, and I. G. Main, Phys. Rev. Lett. **112**, 065501 (2014).

3 N. K. Bourne, Z. Rosenberg, and J. E. Field, J. Appl. Phys. **78**, 3736 (1995).

4 M. Marder, Phys. Rev. Lett. **94**, 048001 (2005).

5 V. N. Nikolaevskii, Int. J. Eng. Sci. **19**, 41 (1998).

6 S. V. Rasorenov, G. I. Kanel, V. E. Fortov, and M. M. Abasehov, High Press. Res. **6**, 225 (1991).

7 N. K. Bourne, J. Millett, and Z. Rosenberg, J. Appl. Phys. **81**, 6670 (1997).

8 D. E. Grady, Mech. Mater. **29**, 181 (1998).

9 R. J. Clifton, Appl. Mech. Rev. **46**, 540 (1993).

10 H. D. Espinosa, Y. Xu, and N. S. Brar, J. Am. Ceram. Soc. **80**, 2061 (1997).

11 R. V. Gibbons and T. J. Ahrens, J. Geophys. Res. **76**, 5489 (1971).

12 G. F. Raiser, J. L.Wise, R. J. Clifton, D. E. Grady, and D. E. Cox, J. Appl. Phys. **75**, 3862 (1994).

[13] D. Chen, H. He, and F. Jing, J. Appl. Phys. **102**, 033519 (2007).

[14] L. B. Freund, *Dynamic fracture mechanics* (Cambridge university press, 1998).

[15] E. Sharon and J. Fineberg, Nature **397**, 333 (1999).

[16] G. Kanel, A. Bogatch, S. Razorenov, and Z. Chen, J. Appl. Phys. **92**, 5045 (2002).

[17] Y. G. Zhang, Z. P. Duan, L. S. Zhang, Z. C. Ou, and F. L. Huang, Exp. Mech. **51**, 247 (2011).

[18] D. P. Dandekar and P. A. Beaulieu, in *Metallurgical and Material Applications of Shock-Wave and High-Strain-Rate Phenomena*, edited by L. E. Murr, K. P. Studhammer, and M. A. Meyers (Dekker, New York, 1995), pp. 211–218.

[19] G. Kanel, S. Rasorenov, and V. Fortov, in *Shock Compression of Condensed Matter*, edited by S. C. Schmidt, R. D. Dick, J. W. Forbes, and D. G. Tasker (Elsevier, Amsterdam, 1992), pp. 451–454.

[20] H. J. Prentice, W. G. Proud, S. M. Walley, and J. E. Field, Int. J. Impact Eng. **38**, 849 (2011).

[21] L. Lu, D. Fan, B. X. Bie, X. X. Ran, M. L. Qi, N. Parab, J. Z. Sun, H. J. Liao, M. C. Hudspeth, B. Claus, et al., Rev. Sci. Instrum. **85**, 076101 (2014).

[22] N. McCormick and J. Lord, Mater. Today **13**, 52 (2010).

[23] D. Fan, L. Lu, B. Li, M. L. Qi, J. C. E, F. Zhao, T. Sun, K. Fezzaa, W. Chen, and S. N. Luo, Rev. Sci. Instr. **85**, 113902 (2014).

[24] J. Fineberg, S. P. Gross, M. Marder, and H. L. Swinney, Phys. Rev. Lett. **67**, 457 (1991).

[25] E. Sharon, S. P. Gross, and J. Fineberg, Phys. Rev. Lett. **76**, 2117 (1996).

[26] J. Scheibert, C. Guerra, F. Célarié, D. Dalmas, and D. Bonamy, Phys. Rev. Lett. **104**, 045501 (2010).

[27] C. Guerra, J. Scheibert, D. Bonamy, and D. Dalmas, Proc. Natl. Acad. Sci. U. S. A. **109**, 390 (2012).

[28] L. Barker and R. E. Hollenbach, J. Appl. Phys. **41**, 4208 (1970).

[29] S. P. Marsh, *LASL Shock Hugoniot Data* (University of California Press, Berkely, 1980).

[30] K. Xia, A. J. Rosakis, H. Kanamori, and J. R. Rice, Science **308**, 681 (2005).

[31] N. Maeda, N. Chen, M. Tirrell, and J. N. Israelachvili, Science **297**, 379 (2002).

[32] T. Li, D. Fan, L. Lu, J. Y. Huang, F. Zhao, M. L. Qi, T. Sun, K. Fezzaa, X. H. Xiao, X. M. Zhou, et al., Carbon **91**, 468 (2015).

[33] H. E. Meijer and L. E. Govaert, Prog. Polym. Sci. **30**, 915 (2005).

[34] D. S. De Focatiis and C. P. Buckley, Polym. **52**, 4045 (2011).

[35] B. R. Lawn, J. Am. Ceram. Soc. **66**, 83 (1983).

[36] D. Rittel and H. Maigre, Mech. Mater. **23**, 229 (1996).

[37] A. A. Griffith, Philos. Trans. R. Soc. Lond. A pp. 163–198 (1921).

[38] N. A. Fleck and J. W. Hutchinson, J. Mech. Phys. Solids **41**, 1825 (1993).

[39] Z. F. Zhang, G. He, J. Eckert, and L. Schultz, Phys. Rev. Lett. **91**, 045505 (2003).

[40] D. Grady, J. Appl. Phys. **53**, 322 (1982).

[41] H. D. Espinosa, Y. Xu, and N. S. Brar, J. Am. Ceram. Soc. **80**, 2074 (1997).

[42] H. Y. Wu, G. Ma, and Y. M. Xia, Mater. Lett. **58**, 3681 (2004).

[43] Z. Zhou, B. Su, Z. Wang, Z. Li, X. Shu, and L. Zhao, Mater. Lett. **109**, 151 (2013).

[44] Y. Partom, Int. J. Impact Eng. **21**, 791 (1998).

[45] J. C. F. Millett and N. K. Bourne, J. Appl. Phys. **95**, 4681 (2004).

[46] N. K. Bourne, J. Millett, and Z. Rosenberg, J. Appl. Phys. **80**, 4328 (1996).